The Proteomics Landscape of Pattern Triggered Immunity in the Arabidopsis Leaf Apoplast

Hsiao-Chun Chen[a], Carter J. Newton[a], Feng Kong [a], Yaochao Zheng,[b] Li Yang[a,c], Yao Yao [b], Brian H. Kvitko[a,c]#

[a]Department of Plant Pathology, University of Georgia, Athens, Georgia, USA

[b]Department of Animal and Dairy Science, Regenerative Bioscience Center, University of Georgia, Athens, Georgia, USA

[c]The Plant Center, University of Georgia, Athens, Georgia, USA

Address correspondence to Brian H. Kvitko, bkvitko@uga.edu.

Short title: PTI proteomics in Arabidopsis leaf apoplast

(i) Summary

The apoplast is a critical interface in plant-pathogen interactions particularly in the context of pattern-triggered immunity (PTI), which is initiated by recognition of microbe-associated molecular patterns (PAMPs). Our study characterizes the proteomic profile of the Arabidopsis apoplast during PTI induced by flg22, a 22 amino acid bacterial flagellin epitope, to elucidate the output of PTI. Apoplastic washing fluid (AWF) was extracted with minimal cytoplasmic contamination for LC-MS/MS analysis. We observed consistent identification of PTI enriched and depleted peptides across replicates with limited correlation between total protein abundance and transcript abundance. We observed topological bias in peptide recovery of receptor-like

kinases with peptides predominantly recovered from their ectodomains. Notably, tetraspanin 8, an exosome marker, was enriched in PTI samples. We additionally confirmed increased concentrations of exosomes during PTI. This study enhances our understanding of the proteomic changes in the apoplast during plant immune responses and lays the groundwork for future investigations into the molecular mechanisms of plant defense under recognition of pathogen patterns.

Key words: Pattern-triggered immunity (PTI), Microbe-associated molecular patterns (MAMPs), Apoplast, Proteomics, Extracellular vesicle, Tetraspanin, flg22

35 **(ii) Introduction**

36 Plants are constantly exposed to microbial pathogens, necessitating the evolution of sophisticated
37 defense mechanisms to ensure survival (Boller and He, 2009; Mott et al., 2014). Pattern-
38 triggered immunity (PTI) represents the first layer of inducible defense, activated by the
39 recognition of conserved microbe-associated molecular patterns (MAMPs) through pattern
40 recognition receptors (PRRs) (Boller and He, 2009). These recognition events trigger a complex
41 regulatory network that initiates a variety of defense responses, including the production of
42 reactive oxygen species, transcriptional reprogramming, and callose deposition (Mott et al.,
43 2014; DeFalco and Zipfel, 2021)PTI serves as a critical barrier to pathogen invasion and
44 underscores the importance of studying the molecular mechanisms that underpin this process
45 (Boller and He, 2009; DeFalco and Zipfel, 2021).

46 The apoplast is the intercellular space that contains gas and water, situated between cell
47 membranes and within cell wall matrix (Farvardin et al., 2020). This compartment serves as a
48 critical battleground for plant-microbe interactions and is the location of colonization by foliar
49 bacteria and many other pathogens (Roussin-Léveillée et al., 2024). The apoplast of plants is
50 typically characterized by limited water and nutrient availability, presenting a challenging
51 environment for microbial proliferation (Freeman and Beattie, 2009; O'Leary et al., 2016; Xin et
52 al., 2016; Aung et al., 2018; Gentzel et al., 2022; Liu et al., 2022; Lovelace et al., 2022). The
53 alteration of the apoplastic environment has been proposed to impact pathogen resistance
54 (Roussin-Léveillée et al., 2024). Studies of apoplastic secreted proteins, peptides, and specialized
55 metabolites have provided some insights into apoplastic defense (Anderson et al., 2014;
56 Delaunois et al., 2014; Martínez-González et al., 2018; Gentzel et al., 2022; Serag et al., 2023).

57 Apoplastic proteins have been found to perform diverse functions, including reinforcing the plant
58 cell wall, signal transduction, and inhibition of microbial growth (Alexandersson et al., 2013;
59 Munzert and Engelsdorf, 2025). Secreted proteins include Pathogenesis-related proteins (PRs),
60 enzymes for cell wall modification, enzymes for generation of reactive oxygen species (ROS)
61 and redox regulatory proteins (van Loon et al., 2006; Camejo et al., 2016; Nishimura, 2016),
62 Secreted proteases, chitinases, and other hydrolytic enzymes can mediate defense by
63 modification of plant or pathogen structural targets or the virulence factor targets such as
64 pathogen effector proteins (Van Der Hoorn, 2008). In addition to secreted proteins, plant
65 extracellular vesicles (P-EVs) are emerging as crucial players in immunity. P-EVs are
66 membrane-bound nanostructures classified into MVBs (multivesicular bodies), EXPO (exocyst-
67 positive organelle), Penetration 1 (Pen1)-positive EVs, vacuoles, and autophagosomes based on
68 their biogenesis (Nemati et al., 2022). They facilitate intercellular and interkingdom
69 communication by transporting bioactive molecules, including proteins and RNAs (Rutter and
70 Innes, 2017; Cai et al., 2019). EVs are implicated in enhancing plant defense through the
71 delivery of immune-related cargo, such as small RNAs and proteins, and contribute to systemic
72 immune signaling (Liu et al., 2021). Exosomes, a type of MVB with a median size of
73 approximately 30-150 nm in *Arabidopsis*, have been characterized as a major subtype of P-EVs
74 (Huang et al., 2021). Notably, markers such as tetraspanin-8 (TET8) have been identified in
75 defense-associated exosomes, highlighting their potential role in coordinating immune responses
76 (Wang et al., 2023).

77 Proteomics approaches using suspension cell culture systems have provided important
78 information of extracellular proteins for understanding the molecular mechanisms involved in
79 pathogen infections (Kaffarnik et al., 2009; Kim et al., 2009). While suspension cell culture

80 systems offer the advantage of limiting cytoplasmic contamination, they do not fully replicate the
81 actual conditions of infection or the specific cellular responses observed in intact tissue apoplast,
82 which are critical for understanding the spatial and temporal dynamics upon pathogens interact.
83 Characterization of apoplastic proteomics typically involve isolating apoplastic washing fluid
84 (AWF), followed by protein identification using techniques such as liquid chromatography-
85 tandem mass spectrometry (LC-MS/MS) (Jung et al., 2008). Isolation of AWF is typically
86 conducted using vacuum or pressure infiltration followed by low-speed centrifugation (Agrawal
87 et al., 2010). This technique is efficient in extracting apoplastic contents while minimizing
88 cytoplasmic contamination. To evaluate potential contamination from cytoplasmic components,
89 several assessments are employed using enzymatic assay or immunoblotting to ensure the purity
90 of the AWF (Delaunois et al., 2013; O'Leary et al., 2016). The dynamic nature of the apoplastic
91 proteome and its response to MAMPs remains an active area of research. The Arabidopsis
92 apoplastic proteomic profile during PTI is not well described. Further investigation into the
93 apoplastic proteome under pre-activated PTI will provide crucial insights into the complex
94 interplay of antimicrobial barrier, ultimately leading to the development of more effective
95 strategies for disease control.

96 In this study, we report the apoplastic proteome of *Arabidopsis thaliana* during PTI induced by
97 flg22 a twenty-two amino acid peptide epitope derived from bacterial flagellin and well-studied
98 MAMP. Apoplastic washing fluid (AWF) was extracted by low-speed centrifugation with
99 minimal cytoplasmic contamination and analyzed using liquid chromatography-tandem mass
100 spectrometry (LC-MS/MS). Our analyses identified proteins significantly enriched or depleted
101 during PTI. We also compared these proteome profiles with publicly available transcriptomics
102 time-course data, providing insights into the dynamics of early and late PTI outputs. Notably, we

observed a marked increase during PTI in the tetraspanin 8 exosome marker and an increased exosomes based on nanoflow cytometry. This study provides a detailed snapshot of the proteomic changes in the *Arabidopsis thaliana* apoplast during PTI elicited by flg22, offering a foundation for understanding the molecular mechanisms governing plant immune responses.

(iii) Results

Apoplastic washing fluid isolation

A total of 130–150 leaves were collected for apoplastic washing fluid (AWF) isolation from each sample. 3.5–5.0 mL of AWF was recovered per sample across both mock and flg22 treatments. Cytoplasmic contamination was assessed by measuring glucose-6-phosphate dehydrogenase (G6PDH) activity in the AWF, compared to total leaf extracts (Figure S1). The average G6PDH activity in the mock treatment was 0.55 mU/mL, and in the flg22 treatment was 0.16 mU/mL, compared to 14.6 mU/mL in the total leaf extract. Both mock and flg22 samples exhibited <5% G6PDH activity relative to the total leaf extract with no statistic difference between mock and flg22 treatments, indicating minimal cytoplasmic contamination.

Principal Component Analysis (PCA) of flg22 and mock samples

The peptide abundances were analyzed across the eight combined samples (Figure S2). The overall distribution of log-transformed peptide abundances showed consistency across replicates. Median $\log_{10}$ peptide abundances were similar between the flg22-treated and mock-treated samples, indicating a reliable dataset for further multivariate analysis. Principal Component Analysis (PCA) was used to examine the proteomic differences between flg22-treated and mock-treated samples (Figure 1). The first two components, Dim1 and Dim2, explained 27.9% and

126 25.9% of the total variance, respectively. The PCA plot revealed clustering based on sample
127 types.
128
129 **Comparison of PTI apoplastic proteins enrichment relative to time course transcript**
130 **profiles**
131 A total of 108 proteins were identified as significantly enriched in flg22-treated samples
132 compared to mock controls (Figure 2). We manually classified these proteins into six groups
133 based on protein annotations in Araport: (1) RLKs/RLPs (Receptor-Like Kinases/Receptor-Like
134 Proteins), (2) redox and redox-associated proteins, (3) hydrolytic enzymes, (4) peptides, (5)
135 extracellular vesicles, and (6) others. To better understand to what degree transcriptional
136 regulation relates to protein abundance we integrated our proteomic data with a published
137 Arabidopsis transcriptomics time course from by Hillmer et al., 2017. Within each category,
138 proteins were ranked by their $\log_2$ fold change (log2FC) from highest to lowest abundance. IOS1
139 and SIF2 were among the most abundant in the RLK/RLP category. Other immune-associated
140 RLKs like RLK902 and several CRKs (Cysteine-rich receptor-like protein kinases) were also
141 enriched (Gao et al., 2024). A considerable number of redox-related proteins, such as
142 peroxidases (PERs) and glutathione-S-transferases (GSTFs) were prominent. Several hydrolytic
143 enzymes were identified in the apoplast during flg22-induced PTI in *Arabidopsis*. Enzymes
144 involved in carbohydrate metabolism, including chitinase family proteins (At1g02360), and beta-
145 hexosaminidase 3 (HEXO3), were enriched. Subtilisin-like protease SBT3.3 and glucan endo-
146 1,3-beta-glucosidase 14 (At2g27500) were also identified, along with related beta-glucosidases.
147 Enzymes involved in cell wall modifications, such as pectin methylesterases (PMEs) and
148 xyloglucan endotransglucosylases, were present in the enriched profile. EARLI1 gene in

149 *Arabidopsis* encodes a lipid transfer protein-like protein that plays a crucial role in mediating
150 systemic defense mechanisms, specifically systemic acquired resistance (SAR) and induced
151 systemic resistance (ISR) were also enriched by flg22 (Vlot et al., 2021). Notably, in flg22-
152 enriched profile, three proteins associated with vesicle trafficking were identified as significantly
153 enriched under PTI conditions. The enriched proteins include Syntaxin of Plants-122 (SYP122),
154 a Qa-SNARE which functions in vesicle fusion with the plasma membrane peptidyl-prolyl cis-
155 trans isomerase FKBP15-1 (FKBP15-1), which may contribute to protein folding within vesicles
156 and tetraspanin-8 (TET8), associated with exosome extracellular vesicle structural integrity
157 (Boavida et al., 2013; Wang et al., 2020; Rubiato et al., 2022).
158
159 The heatmap (Figure 2) illustrates how the transcript abundance changes over time, providing
160 insights into the continuity or discontinuity between transcription and protein accumulation in
161 response to flg22 treatment. The transcriptomic analysis revealed distinct patterns of gene
162 expression in response to flg22 treatment, corresponding with the functional roles of the
163 identified proteins in PTI. There are 21 receptor-like kinases and receptor-like proteins
164 (RLK/RLP) identified in the enriched profile and 10 of them displayed rapid upregulation at the
165 first hours then the expression level gradually decreased. Several redox-related proteins and
166 hydrolytic enzymes, such as peroxidases (PER21, PER52, and PER71) and Glutathione S-
167 Transferase (GSTF6 and GSTF7) showed sustained transcriptional upregulation at a relatively
168 later time point. Overall, within each functional group, protein abundance ratios did not
169 necessarily align with transcriptional trends in a time-course manner.
170
171 **Recovered peptides of RLKs are heavily biased to ectodomains.**

172 RLKs membrane proteins were enriched in the apoplastic proteome after flg22 treatment.
173 Considering that these are transmembrane proteins, we would not expect them be found in the
174 free extracellular fraction. We investigated the topological distribution of detected peptides in 18
175 identified RLKs in our dataset enriched under PTI conditions (Figure 3). This detection pattern
176 shows a notable bias toward the extracellular region, suggesting that portions of these
177 membrane-associated proteins are accessible or released into the apoplast under PTI conditions.
178 Very few peptides were captured close to the cytoplasmic regions. The extracellular bias aligns
179 with the apoplast-specific protein collection procedure. The limited peptide coverage in
180 cytoplasmic regions further emphasize the specificity of the apoplast isolation protocol.
181
182 **flg22 depleted apoplastic proteins displayed limited functional clustering and transcript-**
183 **protein abundance discrepancies.**
184 A total of 255 proteins were identified as significantly depleted following flg22 treatment
185 compared to mock conditions (Figure 4). Unlike the distinct functional clustering observed in the
186 flg22-enriched protein profile, the flg22-depleted proteins did not exhibit clear patterns linked to
187 PTI or disease response functions. However, based on molecular function GO analysis, these
188 proteins were categorized into 10 functional groups. We observed some genes displaying high
189 transcript levels post-flg22 treatment despite their decreased protein abundance in the apoplast,
190 indicating some discontinuity between transcript and protein abundances.
191
192 **Gene Ontology (GO) analysis of the enriched protein profile under the flg22 treatment**
193 We performed Gene Ontology (GO) analyses of the 108 significantly enriched proteins in flg22
194 treatment with TAIR GO Term Enrichment platform. The GO analysis identified significant

195 enrichment of multiple biological processes in flg22-enriched proteins (Figure 5). Processes with
196 the highest gene number include response to stimulus and response to stress, suggesting that
197 many enriched proteins are involved in both general and specific stress responses. More specific
198 processes, such as response to biotic stimulus, defense response to Gram-negative bacterium, and
199 defense response to fungus, highlight these proteins' roles in responding to presence of
200 pathogens. Specific processes such as response to oxygen levels and response to oxidative stress
201 are also enriched, suggesting that these proteins may play roles in reactive oxygen species (ROS)
202 production, which are commonly associated with plant immune responses signaling (Torres et
203 al., 2006). Notably, highly representative pathway with higher fold enrichment like defense
204 response to Gram-negative bacterium align with the expected response to the bacterial elicitor
205 flg22.
206
207 The molecular function analysis for flg22-enriched proteins revealed significant enrichment in
208 various catalytic and kinase activities. Nearly 25% of the proteins identified in the GO analysis
209 were annotated for catalytic activity. The enrichment of oxidoreductase activity, including
210 peroxidase and lactoperoxidase functions, suggests roles associated with redox reactions and
211 potential oxidative stress responses. Proteins with kinase and transferase activities, particularly
212 those transferring phosphorus-containing groups, were also prominent. Specifically, protein
213 kinase activity and protein serine/threonine kinase activity were enriched, indicating involvement
214 in phosphorylation cascades.
215
216 Consistent with an apoplastic proteome, the cellular component analysis for flg22-enriched
217 proteins revealed significant enrichment in regions associated with the cell periphery,

218 extracellular region, and membrane. Nearly 15% of the proteins identified in the GO analysis
219 were localized to the cell periphery, suggesting a strong role in cell surface interactions. Notably,
220 vesicles and components associated with the secretory pathway were also prominent in the
221 dataset. The presence of proteins localized to vesicles, including secretory and cytoplasmic
222 vesicles, underscores their potential involvement in protein trafficking and secretion.
223
224 **PTI is associated with increased numbers of exosomes in leaf apoplast**
225 Several studies have reported the enrichment of plant extracellular vesicles during pathogen
226 infection (Rutter and Innes, 2017; Cai et al., 2019). In our dataset, we observed significantly
227 enriched proteins associated with vesicular export, including SYP122, TET8, and FKBP15-1.
228 SYP122 and TET8 show increased change of 8.0 and 5.2-fold, respectively, relative to the mock
229 condition. Notably, TET8 is an exosome marker involved in exosome stability (Cai et al., 2019;
230 Liu et al., 2024). Exosomes are one of several classes of extracellular vesicle are typically
231 between 50nm-150nm in dimeter and have been associated with the cross-kingdom delivery of
232 small RNA for RNAi. We isolated plant extracellular vesicles (EVs) using ultracentrifugation
233 and quantified them using Nano-flow cytometry. The analysis of EV in both flg22-treated and
234 mock samples reveals that the median size of EVs in flg22-treated samples is 67.8 nm, compared
235 to 70.7 nm in mock samples (Figure 6A). This similarity in size indicates no significant
236 difference between the two conditions, suggesting that the majority of these vesicles fall within
237 the size range characteristic of plant exosomes (Rutter and Innes, 2017; Cai et al., 2019).
238
239 Exosomes were found at 5.1×10^9 particles/mL in the flg22-treated samples, nearly three times
240 higher than the 1.7×10^9 particles/mL observed in the mock samples (Figure 6C). This increased

241 concentration in the flg22 condition aligns well with the 5-fold higher protein levels identified in
242 the flg22/mock proteomics analysis. Exosomes presence in the extracted apoplastic wash fluid
243 (AWF) was confirmed by staining with the lipid dye, CFSE, which highlighted the shape and
244 size characteristic of exosomes (Figure 6D).
245
246 **(iv) Discussion**
247
248 GO analysis of the PTI enriched apoplastic proteome revealed significant enrichment in
249 predicted biological processes such as defense responses to Gram-negative bacteria and
250 oxidative stress. The molecular functions enriched in flg22-treated samples included both kinase
251 and oxidoreductase activities, consistent critical roles of PRRs and redox regulation in plant
252 defense mechanisms. The cellular component GO terms, as would be expected, emphasized the
253 extracellular localization of both enriched and depleted proteins, including the cell wall, plasma
254 membrane, secretory vesicles, and extracellular regions. Unlike the PTI-enriched proteins, which
255 were prominently associated with defense signaling and oxidative stress management, the PTI-
256 depleted proteins displayed functions more broadly related to cellular homeostasis and general
257 secretion mechanisms. This may be due to less cytoplasmic leakage in flg22-treated samples
258 during the collection process (Figure S1) or may reflect an overall shift in molecular function.
259 Notably, more than 18% of depleted proteins were associated with functions related to cell
260 organization and biogenesis, including BRI1 (BRASSINOSTEROID INSENSITIVE 1),
261 indicating the stabilization of BR signaling under naïve conditions, this can potentially be a
262 consequence of the growth-defense trade-off (Huot et al., 2014).
263

264 We defined five functional categories of apoplastic proteins enriched during flg22-triggered PTI,
265 including RLK/RLPs, redox-associated proteins, hydrolytic enzymes, peptides, extracellular
266 vesicle (EV) associated proteins. Among the RLKs, IOS1 (Impaired Oomycete Susceptibility 1)
267 and SIF2 (Stress Induced Factor 2) were highly enriched. These two malectin-domain RLKs
268 have both been observed previously to play roles in PTI signaling. IOS1, a malectin-like leucine-
269 rich repeat RLK, modulates *Arabidopsis* immunity by forming complexes with FLS2 and BAK1
270 to amplify pathogen recognition and defense responses. Loss-of-function mutants of IOS1
271 demonstrate increased susceptibility to bacterial pathogens (Yeh et al., 2016). Similarly, SIF2
272 also interacts with FLS2 and BAK1 and has been implicated in early flg22-triggered immune
273 signaling, contributing to downstream defense activation (Chan et al., 2020). The peptide
274 recovery analysis of RLKs demonstrated a marked bias toward the receptor extracellular regions,
275 with minimal peptides detected in their cytoplasmic regions. The limited recovery of cytoplasmic
276 peptides further aligns with the low levels of cytoplasmic contamination in the apoplastic wash
277 fluid, emphasizing the effectiveness of the apoplast isolation protocol as described by Lovelace
278 et al., 2022. The recovery of free ectodomains in the apoplast may be an artifact of the sampling
279 procedure or could indicate that these ectodomains are endogenously released into the apoplast
280 under the tested conditions through an unknown mechanism.
281
282 A comparative analysis of transcriptome and proteome profiles revealed a complex relationship
283 between transcriptional regulation and endpoint protein abundance during flg22-triggered PTI.
284 For high-abundance proteins, several displayed consistent trends between transcript levels and
285 protein accumulation over the time course. For example, IOS1 and SIF2, both receptor-like
286 kinases (RLKs), exhibited rapid transcriptional upregulation within the first few hours of flg22

287 treatment. This aligns with their role in early pathogen recognition and activation of downstream
288 signaling pathways (Bigeard et al., 2015). Similarly, Peroxidases such as PER15 (Peroxidase
289 15), showed a strong correlation between transcript and protein levels, consistent with its
290 involvement in reactive oxygen species (ROS) management and oxidative stress responses
291 during PTI. However, other high-abundance proteins demonstrated protein enrichment despite
292 declining transcript levels over time. Cysteine-Rich RLKs, another set of RLKs, have distinct
293 patterns of expressions despites their role in response to flg22 perceptions (Yadeta et al., 2017).
294 For instance, CRK11 and CRK12 remained abundant in the apoplast even as their transcript
295 levels decreased after the initial hours of flg22 exposure. On the other hand, CRK13 exhibited
296 decreased transcript levels over time but maintained a high expression pattern and protein
297 abundance during late PTI, suggesting its crucial role in enhanced resistance to bacterial
298 pathogen and is salicylic acid (SA) dependent (Acharya et al., 2007). These suggested post-
299 transcriptional regulatory mechanisms, such as enhanced mRNA stability or protein stabilization,
300 which might prolong the functional presence of critical immune components. Such discrepancies
301 reflect the likely importance of post-transcriptional regulation and protein turnover dynamics in
302 fine-tuning the immune response.
303
304 The enrichment of various hydrolytic enzymes in apoplast in response to flg22 treatment
305 suggested a multifaceted response to PTI. Several enzymes involved in plant cell wall
306 modification were found to be enriched including pectin methyl-esterases (PME3, PME17),
307 xyloglucan endotransglucosylase/hydrolase (XTH23), and β-1,3-glucanases (At2g27500 and
308 At5g56590) (Bethke et al., 2014; Perrot et al., 2022; Zhang et al., 2022). These enzymes
309 collectively suggest that the plant is actively remodeling its cell wall during PTI, possibly to

310 enhance its barrier function against potential pathogens. Several hydrolytic enzymes capable of
311 N-glycosylation of immune receptor and degrading pathogen-associated targets (especially
312 fungal cell wall) were enriched, such as β-hexosaminidase 3 (HEXO3) and endochitinases
313 (At2g43620 and At1g02360) (Liebminger et al., 2011; Fiorin et al., 2018). These enzymes
314 suggest that the plant is actively degrading potential pathogen-derived molecules, which could
315 both weaken a broad-spectrum of pathogens and generate additional immune-stimulating signals.
316 Various proteases and protein-modifying enzymes were also enriched. Metalloendoproteinases
317 (2-MMP and 3-MMP) and subtilisin-like protease (SBT3.3) may be involved in processing
318 defense-related proteins within the extracellular matrix or degrading pathogen-derived proteins
319 (Flinn, 2008; Ramírez et al., 2013; Zhao et al., 2017). Plant aspartyl proteases (MMG4.12 and
320 At3g02740) and cathepsin B-like protease 2 (CATHB2) were also found. These proteases
321 contribute to plant immunity through various mechanisms, from immune signaling activation and
322 systemic resistance to direct cleavage of pathogen proteins (McLellan et al., 2009; Figueiredo et
323 al., 2021). The presence of these proteases suggests active protein processing and turnover,
324 which could be important for the homeostasis of defense signaling molecules and limiting
325 pathogen fitness. Other metabolic enzymes, such as NUDT6 and NUDT7, members of the nudix
326 hydrolase family, were enriched by flg22. They play crucial roles in regulating plant immunity
327 and stress responses by maintaining the redox balance of NADH and acting as ADP-ribose
328 pyrophosphatases (Fonseca and Dong, 2014). The coordinated action of these hydrolytic
329 enzymes with various types of substrates likely contributes to the rapid and effective immune
330 response against potential pathogens, highlighting the sophisticated defense mechanisms
331 employed in pathogen recognition and immune activation.
332

333 The observation of pathogenesis-related 1 (PR1) protein enrichment in the flg22 treatment
334 profile, with a notable 4.67-fold change, strongly aligns with key findings in induced pattern-
335 triggered immunity (PTI). PR1 is a well-established marker for salicylic acid (SA)-regulated
336 plant immunity, and its secretion is critical for activating systemic acquired resistance (SAR).
337 Upon flg22 treatment, plants exhibit increased PR1 expression as part of their PTI
338 response (Djamei et al., 2007). The significant enrichment of PR1 protein abundance observed in
339 this study confirms its responsiveness to PTI triggered by flg22 treatment and further
340 demonstrates the effectiveness of the experimental conditions in inducing a robust immune
341 response.
342
343 For depleted proteins, inconsistencies with transcript levels were even more pronounced. Many
344 of these proteins, such as certain housekeeping enzymes and stress-related factors, exhibited little
345 to no transcriptional change over the time course. Their reduced abundance in the apoplast may
346 result from active degradation, inhibited secretion, or preferential retention in intracellular
347 compartments. Unlike high-abundance proteins, these low-abundance factors were associated
348 with less PTI-relevant processes, further indicating that their depletion may reflect cellular
349 reorganization rather than active participation in immune responses. The integration of
350 transcriptomics and proteomics provides additional insights into the temporal coordination of
351 immune responses. Further time-resolved multi-omics studies could elucidate the functional
352 significance of these regulatory discrepancies, revealing additional layers of complexity in plant
353 immunity.
354

355 Several extracellular vesicle(EVs) -associated proteins exhibited a notable increase in flg22-
356 treated apoplast samples. In particular, tetraspanin-8 (TET8), a well-established exosome marker,
357 was enriched fourfold compared to mock-treated samples. Cai et al., 2018 previously identified
358 TET8 as a core component of exosomes involved in stress responses, and pathogen defense as
359 mediators of interkingdom RNAi. Additionally, the concentration of exosome particles in flg22-
360 treated samples was approximately three times higher than in mock-treated samples. This
361 increase in exosome production suggests enhanced trafficking of defense molecules and
362 signaling factors to the apoplast. The enrichment of Syntaxin-122 (SYP122), a SNARE protein
363 involved in vesicle fusion, supports the idea that vesicle-mediated transport is a key component
364 of the immune response (Waghmare et al., 2018). These results underscore the importance of
365 EVs as critical components of PTI, facilitating intercellular communication and the targeted
366 delivery of antimicrobial proteins and signaling molecules. The substantial enrichment of TET8
367 and the increased exosome particle concentration suggest that EVs play a pivotal role in
368 coordinating and amplifying defense responses during pathogen attack.
369
370 Overall, our study provides a snapshot of the apoplastic proteome in *Arabidopsis* during the later
371 phases of flg22-induced pattern-triggered immunity (PTI). A total of 108 significantly enriched
372 proteins were identified and categorized into key functional groups, including receptor-like
373 kinases/receptor-like proteins (RLK/RLPs), redox-related proteins, hydrolytic enzymes, small
374 peptides, and extracellular vesicle (EV)-associated proteins. Our results highlight the complexity
375 of the apoplastic immune response, where proteins function in distinct stages of PTI activation,
376 defense reinforcement, and signaling. Notably, exosome-associated proteins such as tetraspanin-
377 8 (TET8) were enriched fourfold, and exosome particles increased by approximately threefold.

378 The integration of proteomic and transcriptomic data revealed that transcriptional trends do not
379 always align with protein abundance. This research advances our understanding of the dynamic
380 changes occurring in the apoplast during PTI and underscores the multi-faceted strategies plants
381 employ to defend against pathogen attack. These findings provide a valuable foundation for
382 future investigations into the molecular mechanisms of PTI.
383
384 **(v) Materials and methods**
385 **Plant Tissue Preparation**
386 *A. thaliana* Col-0 seeds suspended in sterile 0.1% agarose were sown in SunGrow 3B
387 Professional potting mix and stratified in darkness for 2 day at 4°C before being grown in a
388 growth chamber (Conviron A1000) with 14-h light (70 μmol) at 22°C. Plants were removed
389 from the chamber at 4 weeks and kept at 12-h day and 12-h night conditions in the growth room
390 prior to apoplastic wash fluid extractions (4.5 weeks).
391
392 **Extraction of Apoplastic Wash Fluid and Cytoplasmic Contamination Measurement**
393 Apoplastic wash fluid (AWF) was crude extracted using vacuum infiltration as described by
394 (Lovelace et al., 2022). 130-150 *A. thaliana* leaves were cut and placed into a 500 mL beaker
395 filled with iced-cold distilled water to top. Repeated cycles of vacuum at 95 kPa for 2 min
396 followed by slow release of pressure were applied until leaves were fully infiltrated. Excess
397 water was blotted from plant tissue before rolled into Saran wrap which were placed into 50 mL
398 conical tubes. Tubes were centrifuged at 1,000 rpm for 10 min at 4°C and the fractions were
399 pooled and stored at -80°C. Cytoplasmic contamination in our AWF samples was examined by
400 comparisons of cytosolic marker glucose-6-phosphate dehydrogenase- G6PDH activity in

401 sampled AWF extracts to the total leaf extracts using standard kit (Sigma-Aldrich, St. Louis,
402 MO, USA). Leaves were homogenized at 4°C. G6PDH activity was assayed
403 spectrophotometrically every 5 min at 37°C where each reaction contained 50 µL of AWF and
404 the activity was calculated according to manufacturer's instructions (Sigma-Aldrich, St. Louis,
405 MO, USA).
406
407 **Sample Preparation and Mass Spectrometry Analysis - LC-MS/MS**
408 Samples were filtered through a 3 kDa Amicon spin filter to approximately 50 µL. The retentate
409 was collected via reverse centrifugation, washed with 50 µL of 50 mM Ammonium bicarbonate,
410 and combined. Total protein content was measured using the Pierce BCA Protein Assay Kit
411 (ThermoFisher Scientific) and quantified at 550 nm based on a BSA standard curve.
412 For digestion, 100 µg of protein from each sample was prepared with the EasyPep Mini MS
413 Sample Prep Kit (ThermoFisher Scientific). After reduction and alkylation at 95°C, samples
414 were digested with Trypsin/LysC (0.2 µg/µL) at 37°C for 2 hours. Digestion was stopped,
415 contaminants removed using peptide cleanup columns, and the eluate was dried and resuspended
416 in 3% acetonitrile/0.1% formic acid. Peptide concentration was measured at 205 nm on a
417 NanoDrop, calculated using an extinction coefficient (Scopes, 1974). Reverse-phase
418 chromatography was performed with water + 0.1% formic acid (A) and 80% acetonitrile + 0.1%
419 formic acid (B). A total of 1 µg of peptides was enriched using a PepMap Neo C18 column,
420 followed by separation on a Vanquish Neo system (Thermo Scientific) with a C18 nanospray
421 column at 45°C. The 90-minute gradient ranged from 1% to 45% B at a flow rate of 300 nL/min,
422 with a final wash at 500 nL/min. Peptides were eluted directly into an Orbitrap Eclipse mass
423 spectrometer with a Nanospray Flex ion source and analyzed in Data Dependent Acquisition

424 mode. MS spectra were collected over m/z 375–2000 in positive mode, with ions of charge state
425 +2 or higher selected for MS/MS. Dynamic exclusion was set to 1 MS/MS per m/z with a 60 s
426 exclusion. MS detection was performed in FT mode at 240,000 resolution, and MS/MS in ion
427 trap mode with HCD collision energy at 30%.
428
429 **Data Analysis and Statistics**
430 Data processing was conducted in Proteome Discoverer (PD) 3.0 (Thermo Scientific). A
431 precursor detector node (S/N=1.5) was used to identify additional precursors within the isolation
432 window for chimeric spectra. Sequest HT searched spectra with methionine oxidation as a
433 dynamic modification and cysteine carbamidomethylating as a fixed modification. An intensity-
434 based rescoring (INFERYS node) using deep learning predicted fragment ion intensities (Zolg et
435 al., 2021). Data were matched against the Arabidopsis thaliana Uniprot proteome
436 (UP000006548) and cRAP contaminants. Searches used a fragment ion tolerance of 0.60 Da and
437 parent ion tolerance of 10 PPM. PSMs were validated by Percolator with FDR ≤1% and protein
438 IDs confirmed by at least one peptide. Log2 fold changes (FC) identified proteins with higher
439 (Log2 FC ≥ 1) or lower (Log2 FC ≤ -1) abundance in flg22 vs. mock, with significance tested
440 using t-tests and Benjamini-Hochberg adjustments.
441
442 **Gene Ontology (GO) Analysis**
443 To identify functional categories enriched in the proteomic data, both significantly enriched
444 proteins and significantly depleted proteins were analyzed using the Gene Ontology (GO)
445 analysis The Arabidopsis Information Resource (TAIR) GO Term Enrichment tool version 2.
446 The analysis was conducted using the TAIR10 genome as the reference dataset to determine

447 over- and under-representation of specific biological processes, molecular functions, and cellular
448 components. Enriched GO terms were considered significant based on a Bonferroni-corrected p-
449 value cutoff of <0.05. The results provided insight into functional trends within the identified
450 apoplastic proteome, including processes associated with plant defense and signal transduction.
451

452 **Transcriptomics analysis**

453 To investigate the transcriptional profiles of Arabidopsis thaliana proteins identified as
454 significantly enriched abundant or significantly depleted abundant in response to flg22 treatment,
455 Tag-Seq data for wild-type Col-0 plants were downloaded from Gene Expression Omnibus
456 (GEO, accession number GSE78735) as described by Hillmer et al., 2017. This dataset included
457 transcriptome profiles collected at seven time points (0, 1, 2, 3, 5, 9, and 18 hours post-
458 infiltration) with three biological replicates per time point. For each gene, the read counts from
459 the three biological replicates were averaged at each time point, normalized to the 0-hour time
460 point by calculating fold changes relative to the average 0-hour value, and log10-transformed.
461 These processed values were visualized as a heatmap using the pheatmap function from the
462 pheatmap package (version 1.0.12) in R.
463

464 **Topology analysis**

465 To analyze the topological distribution of receptor-like kinases (RLKs) in the high-abundance
466 protein profile in response to flg22/mock treatment, peptides identified via Proteome Discoverer
467 (PD) 3.0 were mapped to specific domains or positions within each RLK. Protein domain
468 annotations for the RLKs were obtained from UniProt. Identified peptides corresponding to
469 RLKs were selected and extracted, and their positions were aligned to the respective RLK

470 sequences. This mapping allowed for the determination of peptide coverage within specific
471 protein domains, including extracellular, transmembrane, and intracellular regions.
472
473 **Plant Extracellular vesicle isolation and quantification**
474 The plant extracellular vesicles (P-EVs) isolation was modified from previous studies (Huang et
475 al., 2021). Briefly, the crude AWF was centrifuged for 30 min at 4 °C at 2,000 × g to remove
476 large cell debris, and then the supernatant was further centrifuged at 10,000 × g for 30 minutes at
477 4 °C to remove large insoluble particles. The supernatant (the clean AWF) was then collected
478 and further processed by ultracentrifugation at 100,000 g for 1 hour at 4 °C (Optima™ TLX
479 Ultracentrifuge, Beckman Coulter, Indianapolis, IN) to purify and concentrate P-EVs. Each P-
480 EV pellet was gently resuspended in 50 μL of 0.22nm-filtered PBS, and all samples were
481 aliquoted and stored at -80 °C until further use. Nano-flow cytometry (NFC, NanoFCM, China)
482 was used to analyze P-EVs isolated from both flg22 and mock samples, following the
483 manufacturer's instructions. For each sample, a 0.2 μL aliquot of P-EVs was diluted in 50 μL of
484 filtered PBS (1:250 dilution) for analysis. Particle concentration and size distribution were
485 measured in triplicates. To evaluate differences in exosome biogenesis between the flg22 and
486 mock groups, exosomes yield was calculated as the number of exosomes per gram of leaf tissue
487 used for AWF collection. Statistical analysis was performed using one-way ANOVA to
488 determine exosome yield differences between groups (*P<0.05, **P<0.01, ***P<0.001, NS: not
489 significant).
490
491 Exosomes from mock treatment samples were stained with CFSE dye and examined under
492 confocal microscope. The fluorescence signals were observed by using Zeiss LSM 880 confocal

laser-scanning microscopy. FITC filter (Excitation: 460–500 nm; Emission: 510–560 nm) (Zeiss, Germany) was used to detect the GFP signal (Excitation: 530–560 nm) (Nikon, Tokyo, Japan). Images were generated and merged using The Zen 2.3 imaging software.

(vi) Data statement

The mass spectrometry proteomics data was deposited to the ProteomeXchange with the dataset identifier pending. Details regarding experimental design, sample preparation, and LC-MS/MS parameters are described in the Materials and Methods section of this manuscript.

(vii) Author contributions

HCC, YY, and BHK designed the research; HCC, FK, YZ conducted experiments; HCC, CJN, YZ analyzed the data; and HCC, FK, YZ, and BHK wrote the paper.

(viii) Acknowledgements

This work was supported by the National Science Foundation Grant 1844861 to BK. LY and FK was supported by NIH R35GM143067. We thank Su-Yun Uhm from Department of Genetics, University of Georgia for assistance of Arabidopsis planting and AWF collection. We acknowledge the use of resources provided by the Colorado State University ARC-BIO (Research Resource ID: SCR_021758). Data was generated using the Orbitrap Eclipse Mass Spectrometer were supported by NSF Grant 2117943. We acknowledge the contribution of ARC-BIO staffs- Dorathea Lee for sample preparation and Gustavo Diaz Ph.D. for data analysis.

(x) References

516 **Acharya BR, Raina S, Maqbool SB, Jagadeeswaran G, Mosher SL, Appel HM, Schultz JC,**
517 **Klessig DF, Raina R** (2007) Overexpression of CRK13, an Arabidopsis cysteine-rich
518 receptor-like kinase, results in enhanced resistance to *Pseudomonas syringa*e. The Plant
519 Journal **50**: 488–499
520 **Agrawal GK, Jwa N-S, Lebrun M-H, Job D, Rakwal R** (2010) Plant secretome: Unlocking
521 secrets of the secreted proteins. PROTEOMICS **10**: 799–827
522 **Alexandersson E, Ali A, Resjö S, Andreasson E** (2013) Plant secretome proteomics. Front
523 Plant Sci **4**: 9
524 **Anderson JC, Wan Y, Kim Y-M, Pasa-Tolic L, Metz TO, Peck SC** (2014) Decreased
525 abundance of type III secretion system-inducing signals in Arabidopsis mkp1 enhances
526 resistance against *Pseudomonas syringae*. Proc Natl Acad Sci U S A **111**: 6846–6851
527 **Aung K, Jiang Y, He SY** (2018) The role of water in plant–microbe interactions. The Plant
528 Journal **93**: 771–780
529 **Bethke G, Grundman RE, Sreekanta S, Truman W, Katagiri F, Glazebrook J** (2014)
530 Arabidopsis PECTIN METHYLESTERASEs Contribute to Immunity against *Pseudomonas*
531 *syringae*. Plant Physiology **164**: 1093–1107
532 **Bigeard J, Colcombet J, Hirt H** (2015) Signaling Mechanisms in Pattern-Triggered Immunity
533 (PTI). Molecular Plant **8**: 521–539
534 **Boavida LC, Qin P, Broz M, Becker JD, McCormick S** (2013) Arabidopsis tetraspanins are
535 confined to discrete expression domains and cell types in reproductive tissues and form
536 homo- and heterodimers when expressed in yeast. Plant Physiol **163**: 696–712
537 **Boller T, He SY** (2009) Innate immunity in plants: an arms race between pattern recognition
538 receptors in plants and effectors in microbial pathogens. Science **324**: 742–744

539 **Cai Q, He B, Weiberg A, Buck AH, Jin H** (2019) Small RNAs and extracellular vesicles: New
540 mechanisms of cross-species communication and innovative tools for disease control. PLOS
541 Pathogens **15**: e1008090
542 **Cai Q, Qiao L, Wang M, He B, Lin F-M, Palmquist J, Huang S-D, Jin H** (2018) Plants send
543 small RNAs in extracellular vesicles to fungal pathogen to silence virulence genes. Science
544 **360**: 1126–1129
545 **Camejo D, Guzmán-Cedeño Á, Moreno A** (2016) Reactive oxygen species, essential
546 molecules, during plant-pathogen interactions. Plant Physiol Biochem **103**: 10–23
547 **Chan C, Panzeri D, Okuma E, Tõldsepp K, Wang Y-Y, Louh G-Y, Chin T-C, Yeh Y-H,**
548 **Yeh H-L, Yekondi S, et al** (2020) STRESS INDUCED FACTOR 2 Regulates Arabidopsis
549 Stomatal Immunity through Phosphorylation of the Anion Channel SLAC1. Plant Cell **32**:
550 2216–2236
551 **DeFalco TA, Zipfel C** (2021) Molecular mechanisms of early plant pattern-triggered immune
552 signaling. Molecular Cell **81**: 3449–3467
553 **Delaunois B, Colby T, Belloy N, Conreux A, Harzen A, Baillieul F, Clément C, Schmidt J,**
554 **Jeandet P, Cordelier S** (2013) Large-scale proteomic analysis of the grapevine leaf
555 apoplastic fluid reveals mainly stress-related proteins and cell wall modifying enzymes.
556 BMC Plant Biology **13**: 24
557 **Delaunois B, Jeandet P, Clément C, Baillieul F, Dorey S, Cordelier S** (2014) Uncovering
558 plant-pathogen crosstalk through apoplastic proteomic studies. Front Plant Sci. doi:
559 10.3389/fpls.2014.00249
560 **Djamei A, Pitzschke A, Nakagami H, Rajh I, Hirt H** (2007) Trojan Horse Strategy in
561 Agrobacterium Transformation: Abusing MAPK Defense Signaling. Science **318**: 453–456

562 **Farvardin A, González-Hernández AI, Llorens E, García-Agustín P, Scalschi L, Vicedo B**
563 (2020) The Apoplast: A Key Player in Plant Survival. Antioxidants (Basel) **9**: 604
564 **Figueiredo L, Santos RB, Figueiredo A** (2021) Defense and Offense Strategies: The Role of
565 Aspartic Proteases in Plant–Pathogen Interactions. Biology (Basel) **10**: 75
566 **Fiorin GL, Sanchéz-Vallet A, Thomazella DP de T, Prado PFV do, Nascimento LC do,**
567 **Figueira AV de O, Thomma BPHJ, Pereira GAG, Teixeira PJPL** (2018) Suppression of
568 Plant Immunity by Fungal Chitinase-like Effectors. Current Biology **28**: 3023-3030.e5
569 **Flinn BS** (2008) Plant extracellular matrix metalloproteinases. Functional Plant Biol **35**: 1183–
570 1193
571 **Fonseca JP, Dong X** (2014) Functional Characterization of a Nudix Hydrolase AtNUDX8 upon
572 Pathogen Attack Indicates a Positive Role in Plant Immune Responses. PLOS ONE **9**:
573 e114119
574 **Freeman BC, Beattie GA** (2009) Bacterial Growth Restriction During Host Resistance to
575 *Pseudomonas syringae* Is Associated with Leaf Water Loss and Localized Cessation of
576 Vascular Activity in *Arabidopsis thaliana*. MPMI **22**: 857–867
577 **Gao C, Zhao Y, Wang W, Zhang B, Huang X, Wang Y, Tang D** (2024)
578 BRASSINOSTEROID-SIGNALING KINASE 1 modulates OPEN STOMATA 1
579 phosphorylation and contributes to stomatal closure and plant immunity. The Plant Journal
580 **120**: 45–59
581 **Gentzel I, Giese L, Ekanayake G, Mikhail K, Zhao W, Cocuron J-C, Alonso AP, Mackey D**
582 (2022) Dynamic nutrient acquisition from a hydrated apoplast supports biotrophic
583 proliferation of a bacterial pathogen of maize. Cell Host & Microbe **30**: 502-517.e4

584 **Hillmer RA, Tsuda K, Rallapalli G, Asai S, Truman W, Papke MD, Sakakibara H, Jones**
585 **JDG, Myers CL, Katagiri F** (2017) The highly buffered Arabidopsis immune signaling
586 network conceals the functions of its components. PLoS Genet **13**: e1006639
587 **Huang Y, Wang S, Cai Q, Jin H** (2021) Effective methods for isolation and purification of
588 extracellular vesicles from plants. J Integr Plant Biol **63**: 2020–2030
589 **Huot B, Yao J, Montgomery BL, He SY** (2014) Growth–Defense Tradeoffs in Plants: A
590 Balancing Act to Optimize Fitness. Molecular Plant **7**: 1267–1287
591 **Jung Y-H, Jeong S-H, Kim SH, Singh R, Lee J, Cho Y-S, Agrawal GK, Rakwal R, Jwa N-S**
592 (2008) Systematic Secretome Analyses of Rice Leaf and Seed Callus Suspension-Cultured
593 Cells: Workflow Development and Establishment of High-Density Two-Dimensional Gel
594 Reference Maps. J Proteome Res **7**: 5187–5210
595 **Kaffarnik FAR, Jones AME, Rathjen JP, Peck SC** (2009) Effector Proteins of the Bacterial
596 Pathogen *Pseudomonas syringae* Alter the Extracellular Proteome of the Host Plant,
597 *Arabidopsis thaliana*. Molecular & Cellular Proteomics **8**: 145–156
598 **Kim ST, Kang YH, Wang Y, Wu J, Park ZY, Rakwal R, Agrawal GK, Lee SY, Kang KY**
599 (2009) Secretome analysis of differentially induced proteins in rice suspension-cultured
600 cells triggered by rice blast fungus and elicitor. Proteomics **9**: 1302–1313
601 **Liebminger E, Veit C, Pabst M, Batoux M, Zipfel C, Altmann F, Mach L, Strasser R** (2011)
602 β-N-Acetylhexosaminidases HEXO1 and HEXO3 Are Responsible for the Formation of
603 Paucimannosidic N-Glycans in *Arabidopsis thaliana**. Journal of Biological Chemistry **286**:
604 10793–10802
605 **Liu G, Kang G, Wang S, Huang Y, Cai Q** (2021) Extracellular Vesicles: Emerging Players in
606 Plant Defense Against Pathogens. Front Plant Sci. **12**: 757925

607 **Liu N, Hou L, Chen X, Bao J, Chen F, Cai W, Zhu H, Wang L, Chen X** (2024) Arabidopsis
608 TETRASPANIN8 mediates exosome secretion and glycosyl inositol phosphoceramide
609 sorting and trafficking. The Plant Cell **36**: 626–641
610 **Liu Z, Hou S, Rodrigues O, Wang P, Luo D, Munemasa S, Lei J, Liu J, Ortiz-Morea FA,**
611 **Wang X, et al** (2022) Phytocytokine signalling reopens stomata in plant immunity and
612 water loss. Nature **605**: 332–339
613 **van Loon LC, Rep M, Pieterse CMJ** (2006) Significance of inducible defense-related proteins
614 in infected plants. Annu Rev Phytopathol **44**: 135–162
615 **Lovelace AH, Chen H-C, Lee S, Soufi Z, Bota P, Preston GM, Kvitko BH** (2022) RpoS
616 contributes in a host-dependent manner to *Salmonella* colonization of the leaf apoplast
617 during plant disease. Front Microbiol **13**: 999183
618 **Martínez-González AP, Ardila HD, Martínez-Peralta ST, Melgarejo-Muñoz LM,**
619 **Castillejo-Sánchez MA, Jorrín-Novo JV** (2018) What proteomic analysis of the apoplast
620 tells us about plant–pathogen interactions. Plant Pathology **67**: 1647–1668
621 **McLellan H, Gilroy EM, Yun B-W, Birch PRJ, Loake GJ** (2009) Functional redundancy in
622 the Arabidopsis Cathepsin B gene family contributes to basal defence, the hypersensitive
623 response and senescence. New Phytologist **183**: 408–418
624 **Mott GA, Middleton MA, Desveaux D, Guttman DS** (2014) Peptides and small molecules of
625 the plant-pathogen apoplastic arena. Front Plant Sci. doi: 10.3389/fpls.2014.00677
626 **Munzert KS, Engelsdorf T** (2025) Plant cell wall structure and dynamics in plant–pathogen
627 interactions and pathogen defence. Journal of Experimental Botany **76**: 228–242

628 **Nemati M, Singh B, Mir RA, Nemati M, Babaei A, Ahmadi M, Rasmi Y, Golezani AG,**
629 **Rezaie J** (2022) Plant-derived extracellular vesicles: a novel nanomedicine approach with
630 advantages and challenges. Cell Communication and Signaling **20**: 69
631 **Nishimura M** (2016) Cell wall reorganization during infection in fungal plant pathogens.
632 Physiological and Molecular Plant Pathology **95**: 14–19
633 **O'Leary BM, Neale HC, Geilfus C, Jackson RW, Arnold DL, Preston GM** (2016) Early
634 changes in apoplast composition associated with defence and disease in interactions
635 between *Phaseolus vulgaris* and the halo blight pathogen *Pseudomonas syringae* pv.
636 *phaseolicola*. Plant Cell Environ **39**: 2172–2184
637 **Perrot T, Pauly M, Ramírez V** (2022) Emerging Roles of β-Glucanases in Plant Development
638 and Adaptative Responses. Plants (Basel) **11**: 1119
639 **Ramírez V, López A, Mauch-Mani B, Gil MJ, Vera P** (2013) An Extracellular Subtilase
640 Switch for Immune Priming in Arabidopsis. PLOS Pathogens **9**: e1003445
641 **Roussin-Léveillée C, Mackey D, Ekanayake G, Gohmann R, Moffett P** (2024) Extracellular
642 niche establishment by plant pathogens. Nat Rev Microbiol **22**: 360–372
643 **Rubiato HM, Liu M, O'Connell RJ, Nielsen ME** (2022) Plant SYP12 syntaxins mediate an
644 evolutionarily conserved general immunity to filamentous pathogens. eLife **11**: e73487
645 **Rutter BD, Innes RW** (2017) Extracellular Vesicles Isolated from the Leaf Apoplast Carry
646 Stress-Response Proteins. Plant Physiol **173**: 728–741
647 **Scopes RK** (1974) Measurement of protein by spectrophotometry at 205 nm. Analytical
648 Biochemistry **59**: 277–282

649 **Serag A, Salem MA, Gong S, Wu J-L, Farag MA** (2023) Decoding Metabolic
650 Reprogramming in Plants under Pathogen Attacks, a Comprehensive Review of Emerging
651 Metabolomics Technologies to Maximize Their Applications. Metabolites **13**: 424
652 **Torres MA, Jones JDG, Dangl JL** (2006) Reactive oxygen species signaling in response to
653 pathogens. Plant Physiol **141**: 373–378
654 **Van Der Hoorn RAL** (2008) Plant Proteases: From Phenotypes to Molecular Mechanisms.
655 Annu Rev Plant Biol **59**: 191–223
656 **Vlot AC, Sales JH, Lenk M, Bauer K, Brambilla A, Sommer A, Chen Y, Wenig M, Nayem**
657 **S** (2021) Systemic propagation of immunity in plants. New Phytologist **229**: 1234–1250
658 **Waghmare S, Lileikyte E, Karnik R, Goodman JK, Blatt MR, Jones AME** (2018) SNAREs
659 SYP121 and SYP122 Mediate the Secretion of Distinct Cargo Subsets1. Plant Physiol **178**:
660 1679–1688
661 **Wang J, Sun W, Kong X, Zhao C, Li J, Chen Y, Gao Z, Zuo K** (2020) The peptidyl-prolyl
662 isomerases FKBP15-1 and FKBP15-2 negatively affect lateral root development by
663 repressing the vacuolar invertase VIN2 in Arabidopsis. Planta **252**: 52
664 **Wang Z, Zeng J, Deng J, Hou X, Zhang J, Yan W, Cai Q** (2023) Pathogen-Derived
665 Extracellular Vesicles: Emerging Mediators of Plant-Microbe Interactions. MPMI **36**: 218–
666 227
667 **Xin X-F, Nomura K, Aung K, Velásquez AC, Yao J, Boutrot F, Chang JH, Zipfel C, He SY**
668 (2016) Bacteria establish an aqueous living space in plants crucial for virulence. Nature
669 **539**: 524–529
670 **Yadeta KA, Elmore JM, Creer AY, Feng B, Franco JY, Rufian JS, He P, Phinney B,**
671 **Coaker G** (2017) A Cysteine-Rich Protein Kinase Associates with a Membrane Immune

672 Complex and the Cysteine Residues Are Required for Cell Death1. Plant Physiol **173**: 771–
673 787
674 **Yeh Y-H, Panzeri D, Kadota Y, Huang Y-C, Huang P-Y, Tao C-N, Roux M, Chien H-C,**
675 **Chin T-C, Chu P-W, et al** (2016) The Arabidopsis Malectin-Like/LRR-RLK IOS1 Is
676 Critical for BAK1-Dependent and BAK1-Independent Pattern-Triggered Immunity. The
677 Plant Cell **28**: 1701–1721
678 **Zhang C, He M, Jiang Z, Liu L, Pu J, Zhang W, Wang S, Xu F** (2022) The Xyloglucan
679 Endotransglucosylase/Hydrolase Gene XTH22/TCH4 Regulates Plant Growth by
680 Disrupting the Cell Wall Homeostasis in Arabidopsis under Boron Deficiency. Int J Mol Sci
681 **23**: 1250
682 **Zhao P, Zhang F, Liu D, Imani J, Langen G, Kogel K-H** (2017) Matrix metalloproteinases
683 operate redundantly in Arabidopsis immunity against necrotrophic and biotrophic fungal
684 pathogens. PLoS One **12**: e0183577
685 **Zolg DP, Gessulat S, Paschke C, Graber M, Rathke-Kuhnert M, Seefried F, Fitzemeier K,**
686 **Berg F, Lopez-Ferrer D, Horn D, et al** (2021) INFERYS rescoring: Boosting peptide
687 identifications and scoring confidence of database search results. Rapid Communications in
688 Mass Spectrometry **n/a**: e9128
689

690 **(xi) Figure legends**

691 **Figure 1. Principal Component Analysis (PCA) of flg22 and mock samples.** Clustering of
692 samples indicates distinct profiles between the flg22 and mock treatments with 27.9%variance in
693 dimension 1 and 25.9% in dimension 2.
694

695 **Figure 2. PTI-enriched proteins ranked by functional groups and relative to transcriptome**
696 **profiles.** The heatmap presents flg22-enriched protein abundances on a red scale. The
697 corresponding transcriptome profiles are displayed on a blue-yellow scale, with data are shown
698 at 0, 1, 2, 3, 5, 9, and 18 hours post flg22 treatment relative to mock treatment. Transcriptome
699 data were obtained from study of Hillmer et al., 2017. GEO data series GSE78735.
700
701 **Figure 3. Peptide distribution analysis of receptor-like kinases (RLKs) in flg22-enriched**
702 **proteins.** Identified peptides mapping to PTI enriched receptor-like kinases (RLKs). The
703 majority of peptides are detected from the extracellular regions, while very few are observed in
704 the cytoplasmic regions.
705
706 **Figure 4. PTI-depleted proteins ranked by functional groups and relative to transcriptome**
707 **profiles.** The heatmap illustrates flg22-depleted protein abundances represented on a green scale.
708 Corresponding transcriptomic changes are shown on a yellow-blue scale. Data are displayed
709 across 0, 1, 2, 3, 5, 9, and 18 hours post flg22 treatment relative to mock treatment. Proteins with
710 GO stress responses are bold in font.
711
712 **Figure 5. Gene Ontology (GO) analysis of enriched abundance protein profile.** Dot plot
713 represents significant GO terms of 108 significantly- enriched proteins categorized into cellular
714 component, molecular function, and biological process. The x-axis represents the gene number
715 of each category, while the size of the circles indicates fold enrichment.
716

717 **Figure 6. Plant extracellular vesicles are enriched in flg22 treatment.** (A) Size distribution of
718 flg22-plant EVs identified by Nano-flow cytometry (NFC). (B) Size distribution of mock-P-EVs
719 identified by Nano-flow cytometry (NFC). (C) Comparison of P-EV production between the
720 flg22 and mock groups, showing a significant increase in exosome production in the flg22 group.
721 (D) Confocal images of CFSE-stained exosomes from mock samples. Scale bar=50μm
722
723
724

(xii) Figures

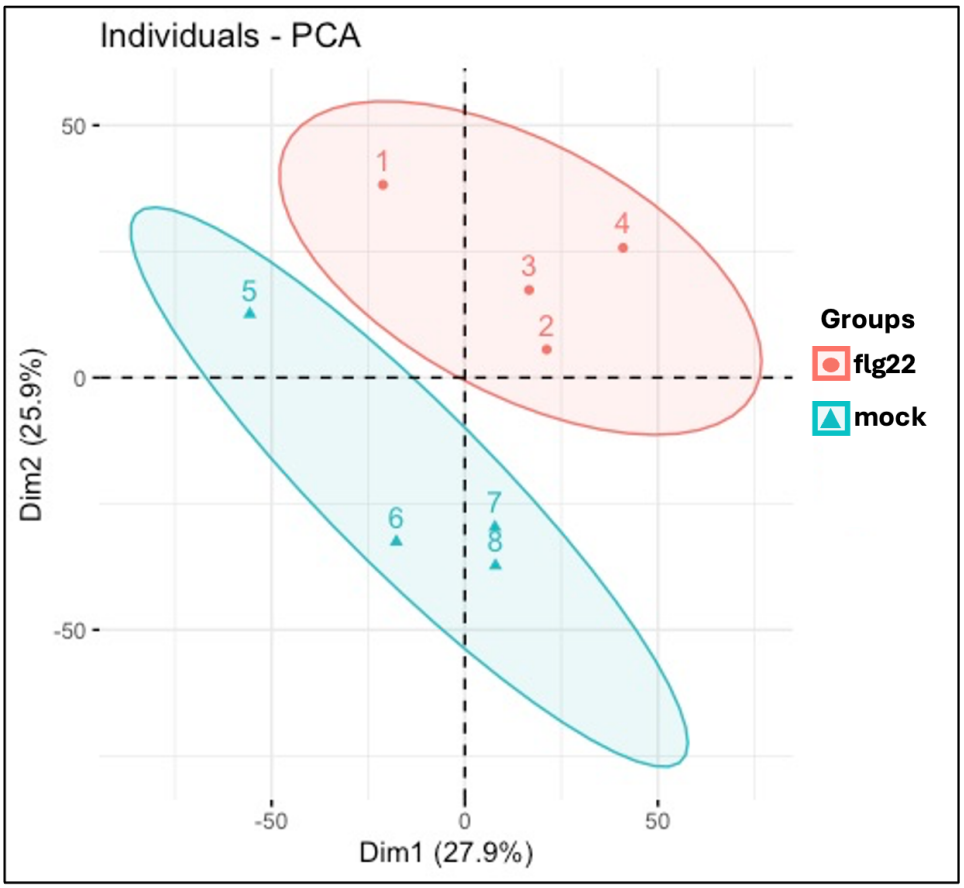
Individuals - PCA
50
0
-50
Dim2 (25.9%)
-50
0
50
Dim1 (27.9%)
1
2
3
4
5
6
7
8
Groups
flg22
mock

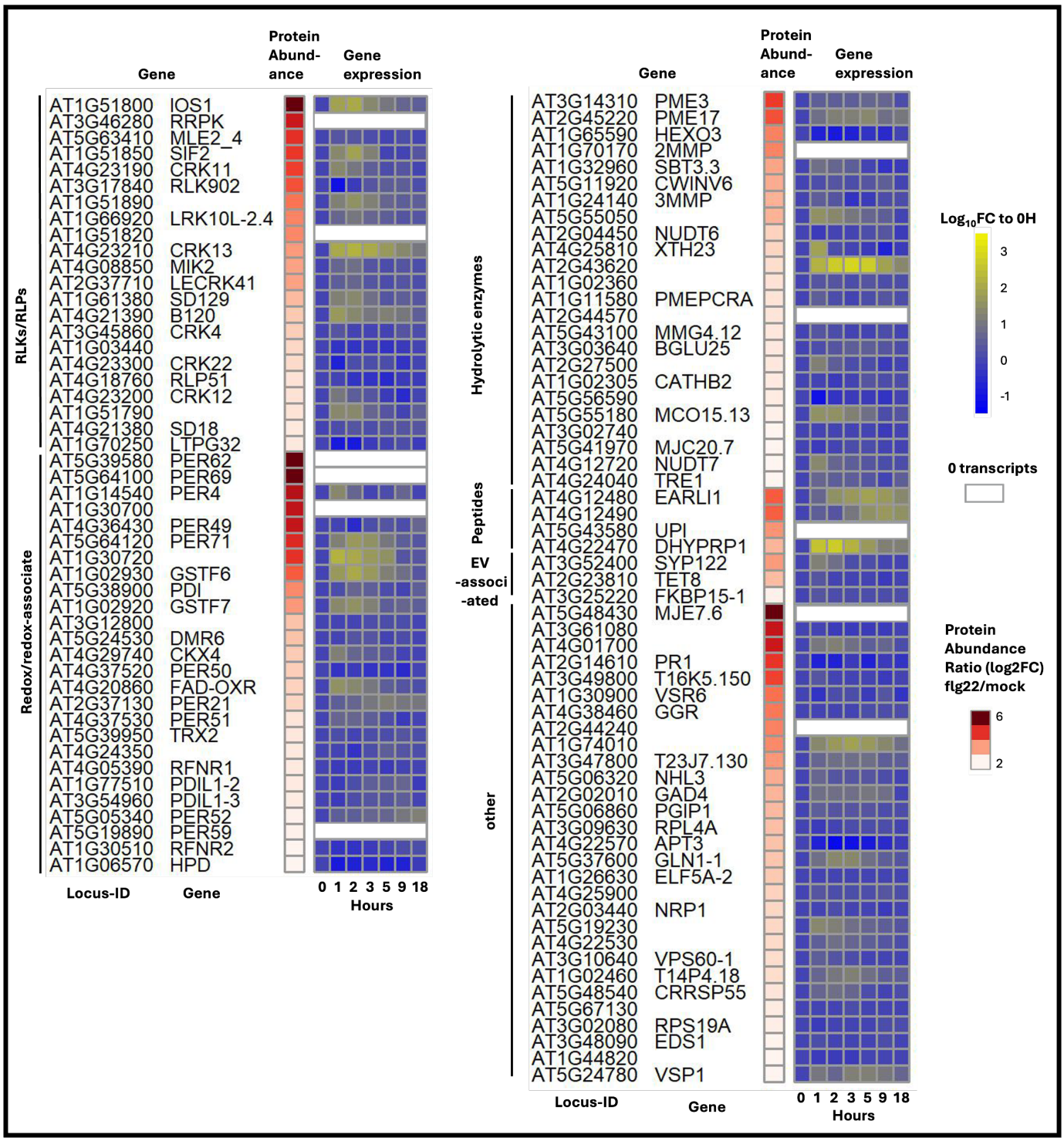
Gene
Protein Abund-ance
Gene expression
RLKs/RLPs
Redox/redox-associate
AT1G51800 IOS1
AT3G46280 RRPK
AT5G63410 MLE2_4
AT1G51850 SIF2
AT4G23190 CRK11
AT3G17840 RLK902
AT1G51890
AT1G66920 LRK10L-2.4
AT1G51820
AT4G23210 CRK13
AT4G08850 MIK2
AT2G37710 LECRK41
AT1G61380 SD129
AT4G21390 B120
AT3G45860 CRK4
AT1G03440
AT4G23300 CRK22
AT4G18760 RLP51
AT4G23200 CRK12
AT1G51790
AT4G21380 SD18
AT1G70250 LTPG32
AT5G39580 PER62
AT5G64100 PER69
AT1G14540 PER4
AT1G30700
AT4G36430 PER49
AT5G64120 PER71
AT1G30720
AT1G02930 GSTF6
AT5G38900 PDI
AT1G02920 GSTF7
AT3G12800
AT5G24530 DMR6
AT4G29740 CKX4
AT4G37520 PER50
AT4G20860 FAD-OXR
AT2G37130 PER21
AT4G37530 PER51
AT5G39950 TRX2
AT4G24350
AT4G05390 RFNR1
AT1G77510 PDIL1-2
AT3G54960 PDIL1-3
AT5G05340 PER52
AT5G19890 PER59
AT1G30510 RFNR2
AT1G06570 HPD
Locus-ID
Gene
0 1 2 3 5 9 18
Hours
Hydrolytic enzymes
Peptides
EV -associ -ated
other
AT3G14310 PME3
AT2G45220 PME17
AT1G65590 HEXO3
AT1G70170 2MMP
AT1G32960 SBT3.3
AT5G11920 CWINV6
AT1G24140 3MMP
AT5G55050
AT2G04450 NUDT6
AT4G25810 XTH23
AT2G43620
AT1G02360
AT1G11580 PMEPCRA
AT2G44570
AT5G43100 MMG4.12
AT3G03640 BGLU25
AT2G27500
AT1G02305 CATHB2
AT5G56590
AT5G55180 MCO15.13
AT3G02740
AT5G41970 MJC20.7
AT4G12720 NUDT7
AT4G24040 TRE1
AT4G12480 EARLI1
AT4G12490
AT5G43580 UPI
AT4G22470 DHYPRP1
AT3G52400 SYP122
AT2G23810 TET8
AT3G25220 FKBP15-1
AT5G48430 MJE7.6
AT3G61080
AT4G01700
AT2G14610 PR1
AT3G49800 T16K5.150
AT1G30900 VSR6
AT4G38460 GGR
AT2G44240
AT1G74010
AT3G47800 T23J7.130
AT5G06320 NHL3
AT2G02010 GAD4
AT5G06860 PGIP1
AT3G09630 RPL4A
AT4G22570 APT3
AT5G37600 GLN1-1
AT1G26630 ELF5A-2
AT4G25900
AT2G03440 NRP1
AT5G19230
AT4G22530
AT3G10640 VPS60-1
AT1G02460 T14P4.18
AT5G48540 CRRSP55
AT5G67130
AT3G02080 RPS19A
AT3G48090 EDS1
AT1G44820
AT5G24780 VSP1
Log10FC to 0H
3
2
1
0
-1
0 transcripts
Protein Abundance Ratio (log2FC) flg22/mock
6
2

730

731

732

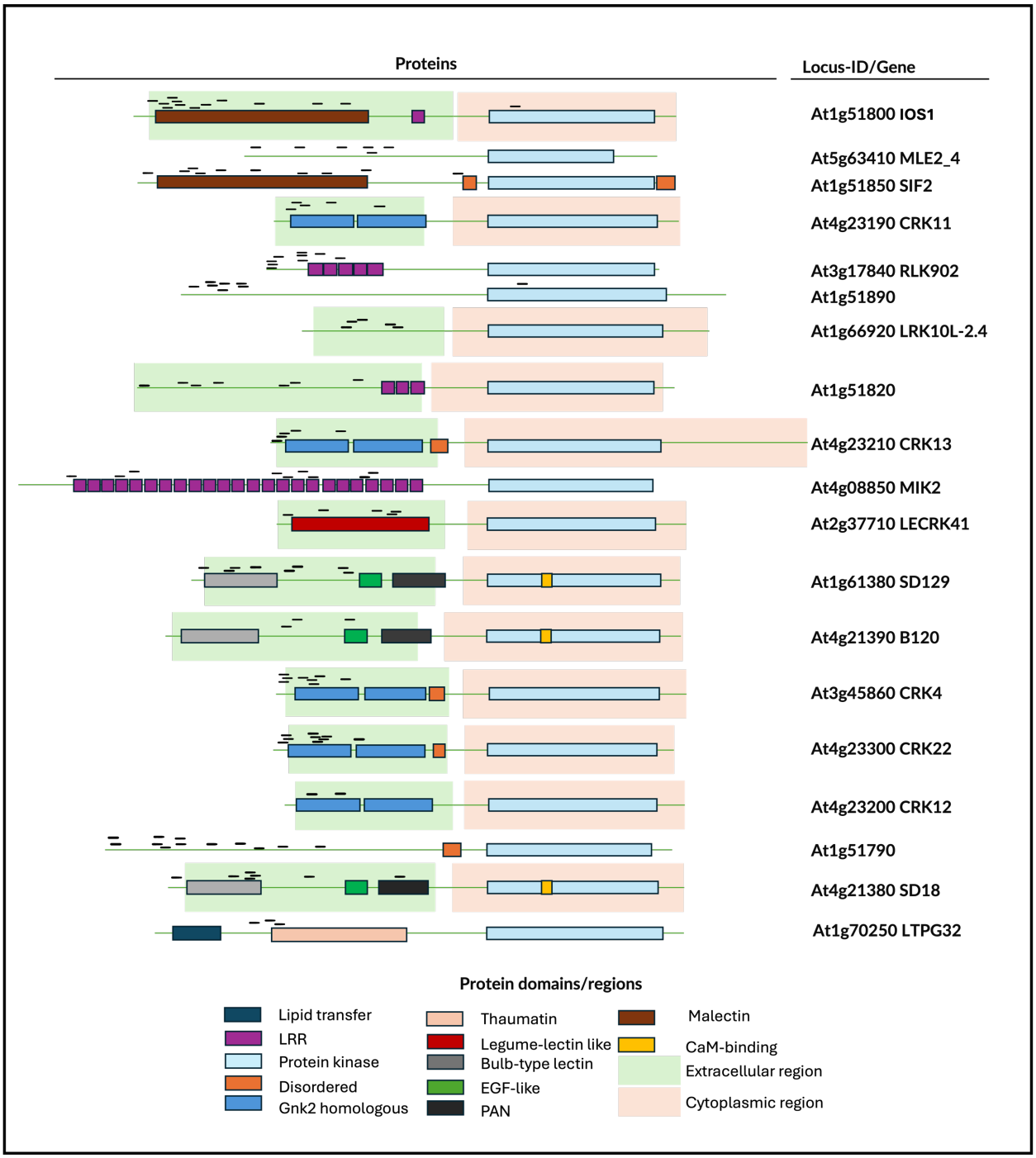
Proteins
Locus-ID/Gene
At1g51800 IOS1
At5g63410 MLE2_4
At1g51850 SIF2
At4g23190 CRK11
At3g17840 RLK902
At1g51890
At1g66920 LRK10L-2.4
At1g51820
At4g23210 CRK13
At4g08850 MIK2
At2g37710 LECRK41
At1g61380 SD129
At4g21390 B120
At3g45860 CRK4
At4g23300 CRK22
At4g23200 CRK12
At1g51790
At4g21380 SD18
At1g70250 LTPG32
Protein domains/regions
Lipid transfer
LRR
Protein kinase
Disordered
Gnk2 homologous
Thaumatin
Legume-lectin like
Bulb-type lectin
EGF-like
PAN
Malectin
CaM-binding
Extracellular region
Cytoplasmic region

733

734

735

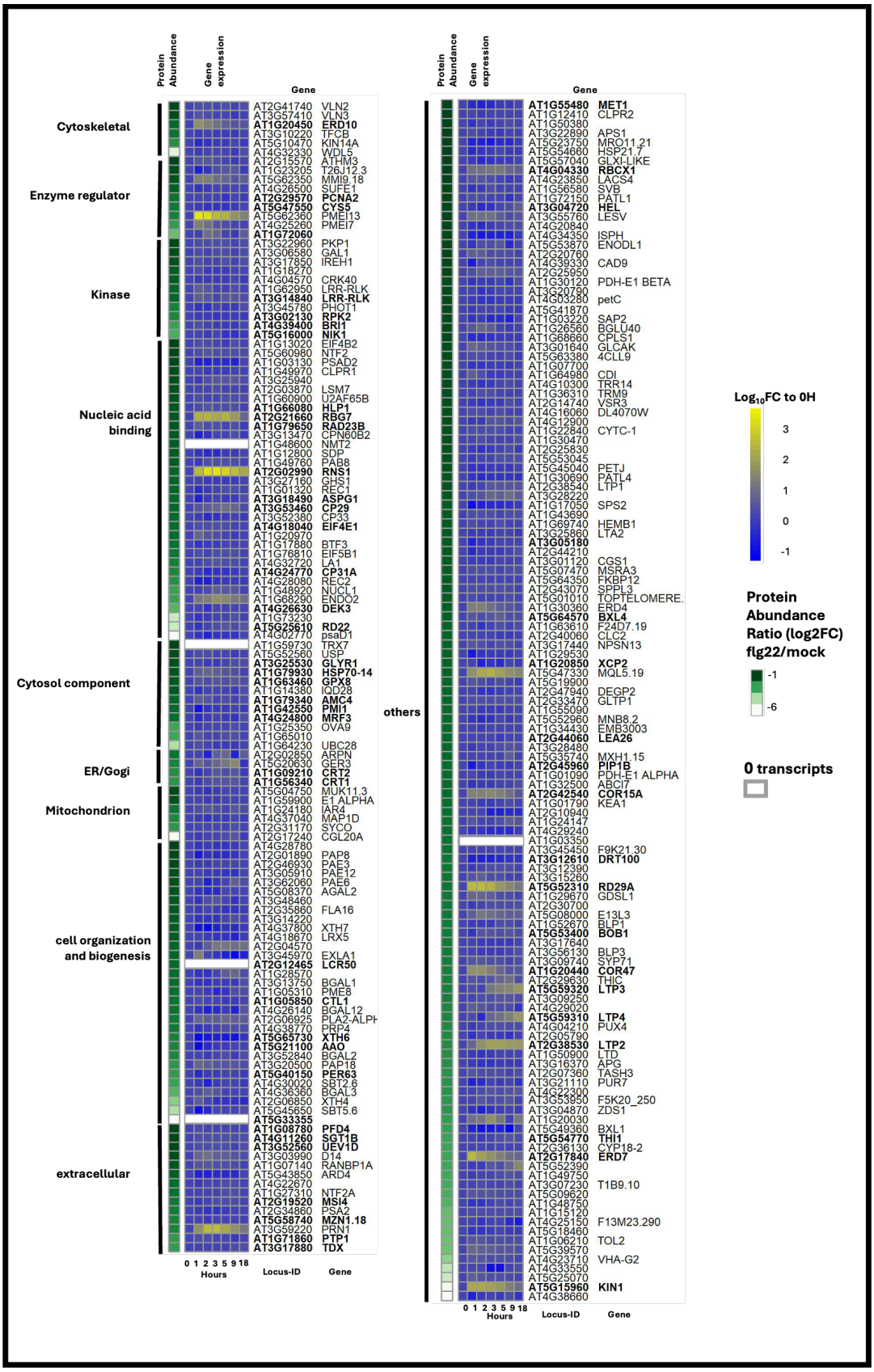
Protein Abundance
Gene expression
Gene
Cytoskeletal
Enzyme regulator
Kinase
Nucleic acid binding
Cytosol component
ER/Gogi
Mitochondrion
cell organization and biogenesis
extracellular
AT2G41740 VLN2
AT3G57410 VLN3
AT1G20450 ERD10
AT3G10220 TFCB
AT5G10470 KIN14A
AT4G32330 WDL5
AT2G15570 ATHM3
AT1G23205 T26J12.3
AT5G62350 MMI9.18
AT4G26500 SUFE1
AT2G29570 PCNA2
AT5G47550 CYS5
AT5G62360 PMEI13
AT4G25260 PMEI7
AT1G72060
AT3G22960 PKP1
AT3G06580 GAL1
AT3G17850 IREH1
AT1G18270
AT4G04570 CRK40
AT1G62950 LRR-RLK
AT3G14840 LRR-RLK
AT3G45780 PHOT1
AT3G02130 RPK2
AT4G39400 BRI1
AT5G16000 NIK1
AT1G13020 EIF4B2
AT5G60980 NTF2
AT1G03130 PSAD2
AT1G49970 CLPR1
AT3G25840
AT2G03870 LSM7
AT1G60900 U2AF65B
AT1G66080 HLP1
AT2G21660 RBG7
AT1G79650 RAD23B
AT3G13470 CPN60B2
AT1G48600 NMT2
AT1G12800 SDP
AT1G49760 PAB8
AT2G02990 RNS1
AT3G27160 GHS1
AT1G01320 REC1
AT3G18490 ASPG1
AT3G53460 CP29
AT3G52380 CP33
AT4G18040 EIF4E1
AT1G20970
AT1G17880 BTF3
AT1G76810 EIF5B1
AT4G32720 LA1
AT4G24770 CP31A
AT4G28080 REC2
AT1G48920 NUCL1
AT1G68290 ENDO2
AT4G26630 DEK3
AT1G73230
AT5G25610 RD22
AT4G02770 psaD1
AT1G59730 TRX7
AT5G52560 USP
AT3G25530 GLYR1
AT1G79930 HSP70-14
AT1G63460 GPX8
AT1G14380 IQD28
AT1G79340 AMC4
AT1G42550 PMI1
AT4G24800 MRF3
AT1G25350 OVA9
AT1G65010
AT1G64230 UBC28
AT2G02850 ARPN
AT5G20630 GER3
AT1G09210 CRT2
AT1G56340 CRT1
AT5G04750 MUK11.3
AT1G59900 E1 ALPHA
AT1G24180 IAR4
AT4G37040 MAP1D
AT2G31170 SYCO
AT2G17240 CGL20A
AT4G28780
AT2G01890 PAP8
AT2G46930 PAE3
AT3G05910 PAE12
AT3G62060 PAE6
AT5G08370 AGAL2
AT3G48460
AT2G35860 FLA16
AT3G14220
AT4G37800 XTH7
AT4G18670 LRX5
AT2G04570
AT3G45970 EXLA1
AT2G12465 LCR50
AT1G28570
AT3G13750 BGAL1
AT1G05310 PME8
AT1G05850 CTL1
AT4G26140 BGAL12
AT2G06925 PLA2-ALPH
AT4G38770 PRP4
AT5G65730 XTH6
AT5G21100 AAO
AT3G52840 BGAL2
AT3G20500 PAP18
AT5G40150 PER63
AT4G30020 SBT2.6
AT4G36360 BGAL3
AT2G06850 XTH4
AT5G45650 SBT5.6
AT5G33355
AT1G08780 PFD4
AT4G11260 SGT1B
AT3G52560 UEV1D
AT3G03990 D14
AT1G07140 RANBP1A
AT5G43850 ARD4
AT4G22670
AT1G27310 NTF2A
AT2G19520 MSI4
AT2G34860 PSA2
AT5G58740 MZN1.18
AT3G59220 PRN1
AT1G71860 PTP1
AT3G17880 TDX
0 1 2 3 5 9 18
Hours
Locus-ID
Gene
others
AT1G55480 MET1
AT1G12410 CLPR2
AT1G50380
AT3G22890 APS1
AT5G23750 MRO11.21
AT5G54660 HSP21.7
AT5G57040 GLXI-LIKE
AT4G04330 RBCX1
AT4G23850 LACS4
AT1G56580 SVB
AT1G72150 PATL1
AT3G04720 HEL
AT3G55760 LESV
AT4G20840
AT4G34350 ISPH
AT5G53870 ENODL1
AT2G20760
AT4G39330 CAD9
AT2G25950
AT1G30120 PDH-E1 BETA
AT3G20780
AT4G03280 petC
AT5G41870
AT1G03220 SAP2
AT1G26560 BGLU40
AT1G68660 CPLS1
AT3G01640 GLCAK
AT5G63380 4CLL9
AT1G07700
AT1G64980 CDI
AT4G10300 TRR14
AT1G36310 TRM9
AT2G14740 VSR3
AT4G16060 DL4070W
AT4G12900
AT1G22840 CYTC-1
AT1G30470
AT2G25830
AT5G53045
AT5G45040 PETJ
AT1G30690 PATL4
AT2G38540 LTP1
AT3G28220
AT1G17050 SPS2
AT1G43890
AT1G69740 HEMB1
AT3G25860 LTA2
AT3G05180
AT2G44210
AT3G01120 CGS1
AT5G07470 MSRA3
AT5G64350 FKBP12
AT2G43070 SPPL3
AT5G01010 TOPTELOMERE.
AT1G30360 ERD4
AT5G64570 BXL4
AT1G63610 F24D7.19
AT2G40060 CLC2
AT3G17440 NPSN13
AT1G29530
AT4G20850 XCP2
AT5G47330 MQL5.19
AT5G19900
AT2G47940 DEGP2
AT2G33470 GLTP1
AT1G55090
AT5G52960 MNB8.2
AT1G34430 EMB3003
AT2G44060 LEA26
AT3G28480
AT5G35740 MXH1.15
AT2G45960 PIP1B
AT1G01090 PDH-E1 ALPHA
AT1G32500 ABCI7
AT2G42540 COR15A
AT1G01790 KEA1
AT2G10940
AT1G24147
AT4G29240
AT1G03350
AT3G45450 F9K21.30
AT3G12610 DRT100
AT3G12390
AT3G15260
AT5G52310 RD29A
AT1G29670 GDSL1
AT2G30700
AT5G08000 E13L3
AT1G52670 BLP1
AT5G53400 BOB1
AT3G17640
AT3G56130 BLP3
AT3G09740 SYP71
AT1G20440 COR47
AT2G29630 THIC
AT5G59320 LTP3
AT3G09250
AT4G29020
AT5G59310 LTP4
AT4G04210 PUX4
AT2G05790
AT2G38530 LTP2
AT1G50900 LTD
AT3G16370 APG
AT2G07360 TASH3
AT3G21110 PUR7
AT4G22300
AT3G53950 F5K20_250
AT3G04870 ZDS1
AT1G20030
AT5G49360 BXL1
AT5G54770 THI1
AT2G36130 CYP18-2
AT2G17840 ERD7
AT5G52390
AT1G49750
AT3G07230 T1B9.10
AT5G09620
AT1G48750
AT1G15120
AT4G25150 F13M23.290
AT5G18460
AT1G06210 TOL2
AT5G39570
AT4G23710 VHA-G2
AT4G33550
AT5G25070
AT5G15960 KIN1
AT4G38660
0 1 2 3 5 9 18
Hours
Locus-ID
Gene
Log10FC to 0H
3
2
1
0
-1
Protein Abundance Ratio (log2FC) flg22/mock
-1
-6
0 transcripts

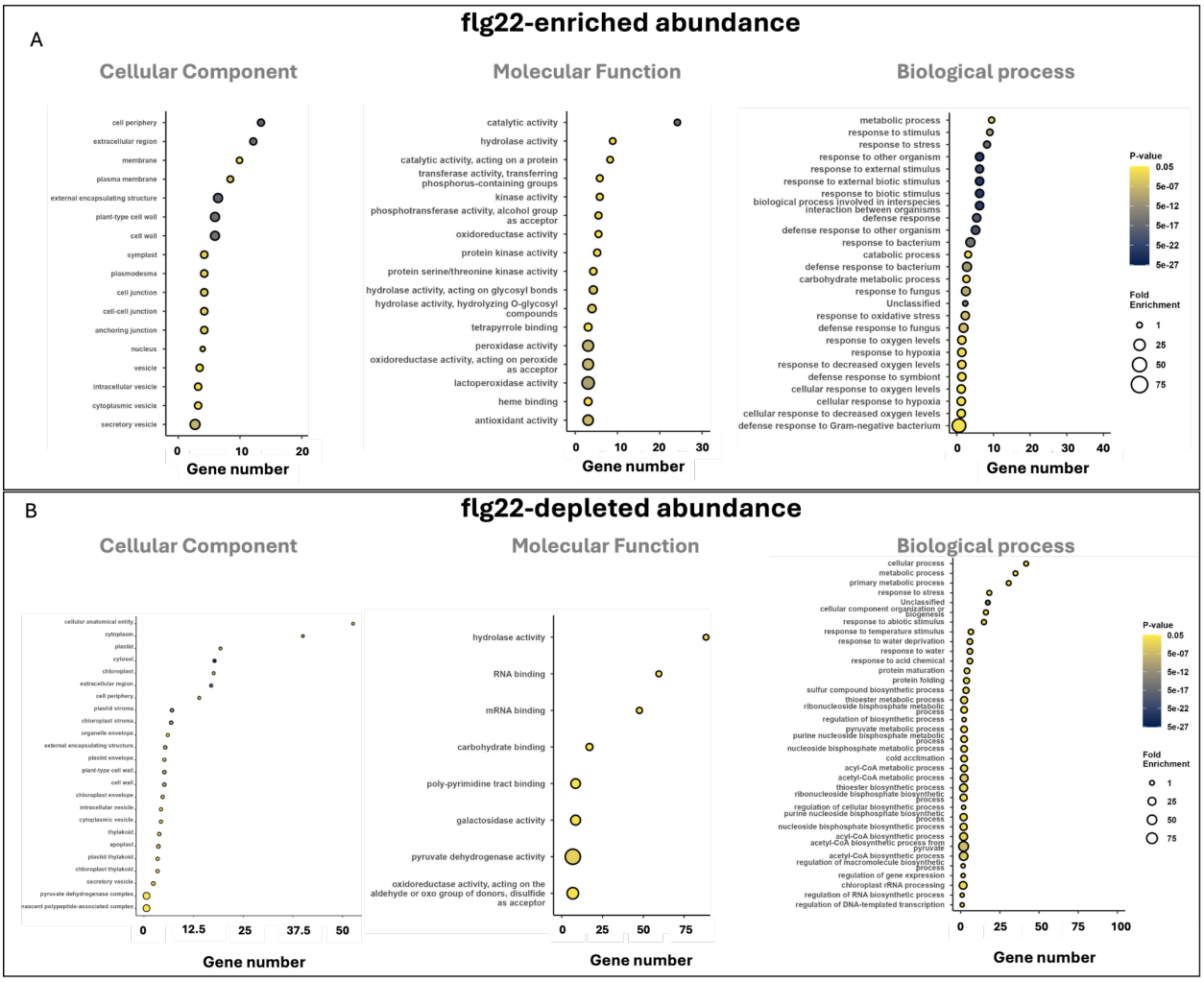
A
flg22-enriched abundance
Cellular Component
cell periphery
extracellular region
membrane
plasma membrane
external encapsulating structure
plant-type cell wall
cell wall
symplast
plasmodesma
cell junction
cell-cell junction
anchoring junction
nucleus
vesicle
intracellular vesicle
cytoplasmic vesicle
secretory vesicle
0
10
20
Gene number
Molecular Function
catalytic activity
hydrolase activity
catalytic activity, acting on a protein
transferase activity, transferring phosphorus-containing groups
kinase activity
phosphotransferase activity, alcohol group as acceptor
oxidoreductase activity
protein kinase activity
protein serine/threonine kinase activity
hydrolase activity, acting on glycosyl bonds
hydrolase activity, hydrolyzing O-glycosyl compounds
tetrapyrrole binding
peroxidase activity
oxidoreductase activity, acting on peroxide as acceptor
lactoperoxidase activity
heme binding
antioxidant activity
0
10
20
30
Gene number
Biological process
metabolic process
response to stimulus
response to stress
response to other organism
response to external stimulus
response to external biotic stimulus
response to biotic stimulus
biological process involved in interspecies interaction between organisms
defense response
defense response to other organism
response to bacterium
catabolic process
defense response to bacterium
carbohydrate metabolic process
response to fungus
Unclassified
response to oxidative stress
defense response to fungus
response to oxygen levels
response to hypoxia
response to decreased oxygen levels
defense response to symbiont
cellular response to oxygen levels
cellular response to hypoxia
cellular response to decreased oxygen levels
defense response to Gram-negative bacterium
0
10
20
30
40
Gene number
P-value
0.05
5e-07
5e-12
5e-17
5e-22
5e-27
Fold Enrichment
1
25
50
75
B
flg22-depleted abundance
Cellular Component
cellular anatomical entity
cytoplasm
plastid
cytosol
chloroplast
extracellular region
cell periphery
plastid stroma
chloroplast stroma
organelle envelope
external encapsulating structure
plastid envelope
plant-type cell wall
cell wall
chloroplast envelope
intracellular vesicle
cytoplasmic vesicle
thylakoid
apoplast
plastid thylakoid
chloroplast thylakoid
secretory vesicle
pyruvate dehydrogenase complex
nascent polypeptide-associated complex
0
12.5
25
37.5
50
Gene number
Molecular Function
hydrolase activity
RNA binding
mRNA binding
carbohydrate binding
poly-pyrimidine tract binding
galactosidase activity
pyruvate dehydrogenase activity
oxidoreductase activity, acting on the aldehyde or oxo group of donors, disulfide as acceptor
0
25
50
75
Gene number
Biological process
cellular process
metabolic process
primary metabolic process
response to stress
Unclassified
cellular component organization or biogenesis
response to abiotic stimulus
response to temperature stimulus
response to water deprivation
response to water
response to acid chemical
protein maturation
protein folding
sulfur compound biosynthetic process
thioester metabolic process
ribonucleoside bisphosphate metabolic process
regulation of biosynthetic process
pyruvate metabolic process
purine nucleoside bisphosphate metabolic process
nucleoside bisphosphate metabolic process
cold acclimation
acyl-CoA metabolic process
acetyl-CoA metabolic process
thioester biosynthetic process
ribonucleoside bisphosphate biosynthetic process
regulation of cellular biosynthetic process
purine nucleoside bisphosphate biosynthetic process
nucleoside bisphosphate biosynthetic process
acyl-CoA biosynthetic process
acetyl-CoA biosynthetic process from pyruvate
acetyl-CoA biosynthetic process
regulation of macromolecule biosynthetic process
regulation of gene expression
chloroplast rRNA processing
regulation of RNA biosynthetic process
regulation of DNA-templated transcription
0
25
50
75
100
Gene number
P-value
0.05
5e-07
5e-12
5e-17
5e-22
5e-27
Fold Enrichment
1
25
50
75

738

739

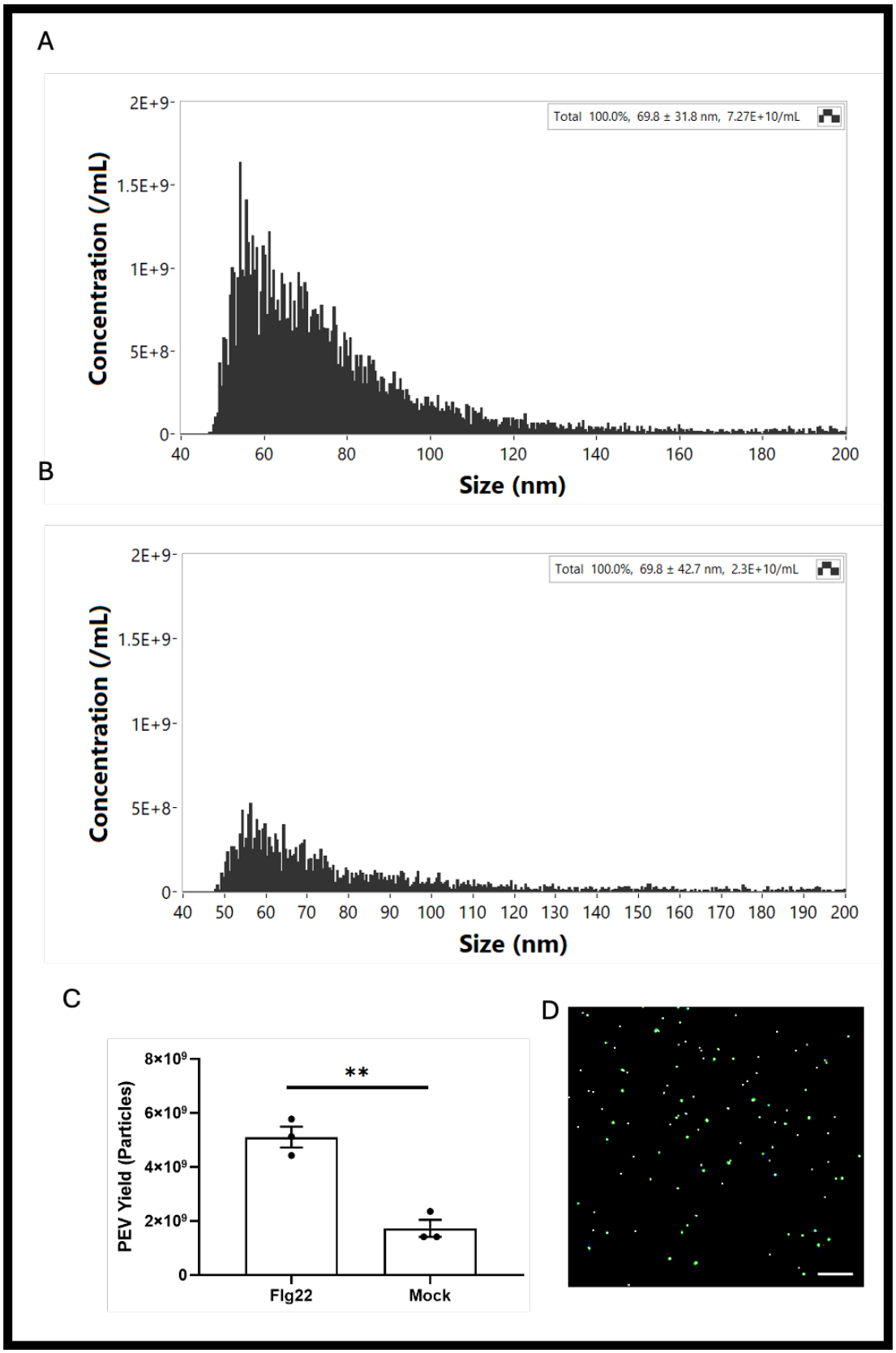
A
Total 100.0%, 69.8 ± 31.8 nm, 7.27E+10/mL
Concentration (/mL)
2E+9
1.5E+9
1E+9
5E+8
0
40
60
80
100
120
140
160
180
200
Size (nm)
B
Total 100.0%, 69.8 ± 42.7 nm, 2.3E+10/mL
Concentration (/mL)
2E+9
1.5E+9
1E+9
5E+8
0
40
50
60
70
80
90
100
110
120
130
140
150
160
170
180
190
200
Size (nm)
C
PEV Yield (Particles)
8×10⁹
6×10⁹
4×10⁹
2×10⁹
0
**
Flg22
Mock
D

740

741

742 **Supporting figures/legends:**

743

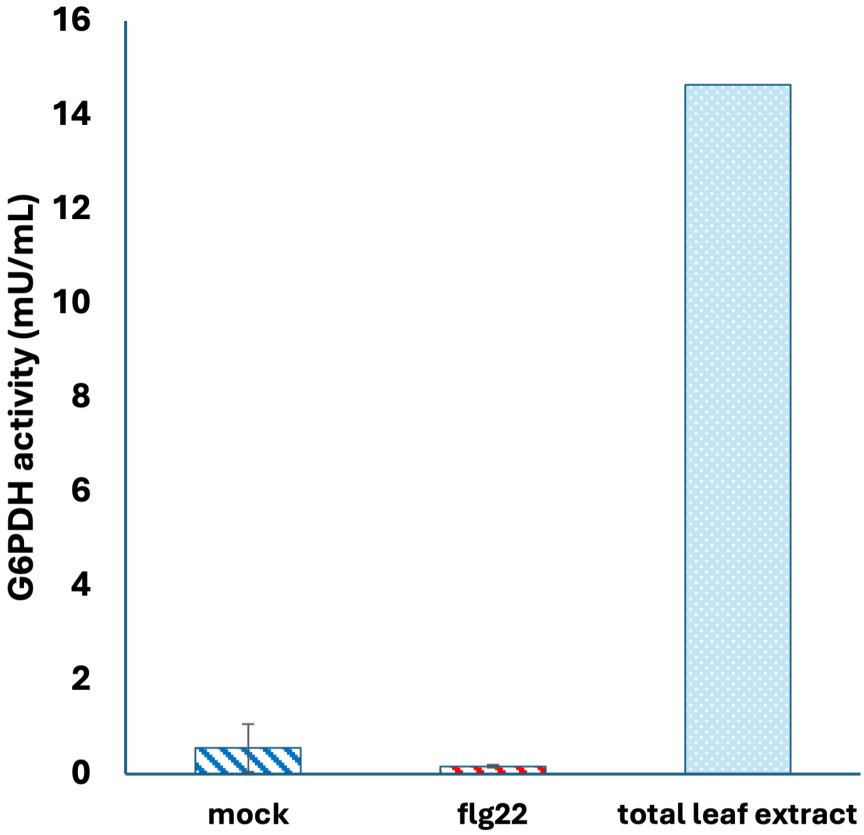

744

745 **Figure S1. Cytoplasmic contamination detection of AWF.** Glucose-6-phosphate

746 dehydrogenase (G6PDH) enzymatic activity of apoplastic washing fluid was tested for

747 cytoplasmic contamination in mock (blue stripe) or flg22 (red stripe) treatment compared to

748 macerated sample (solid).

749

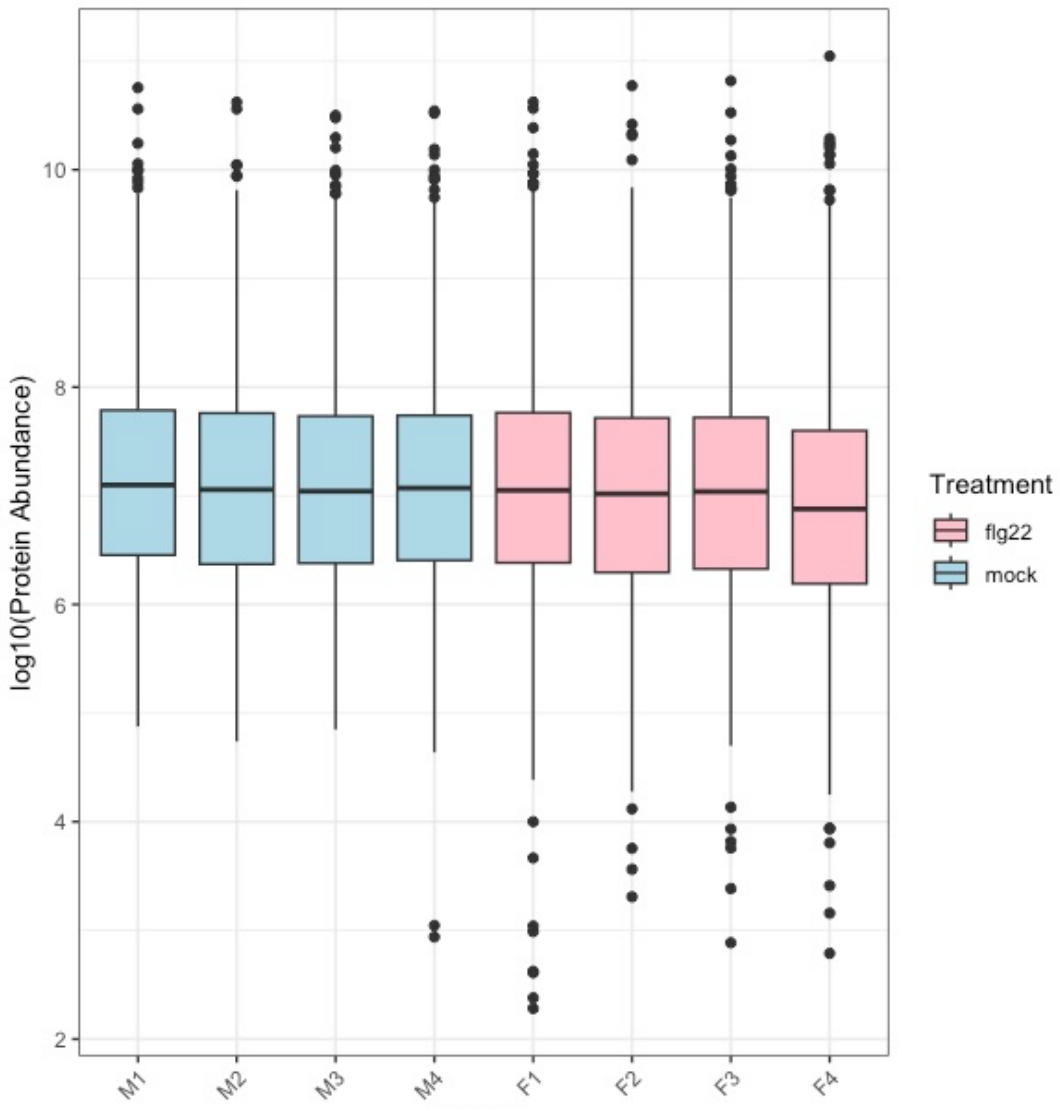

Figure S2. Normalized protein abundances (Log10 transformed data) per sample. Mock treatments are represented in blue boxes (M1-M4) and flg22 treatments are represented in pink boxes (F1-F4). Y-axis represented the log10 transformed of protein abundance.